

Photodissociation of H_2 in Protogalaxies: Modeling Self-Shielding in 3D Simulations

J. Wolcott-Green^{1,3}, Z. Haiman² and G. L. Bryan^{2*}

¹*Columbia Astrophysics Laboratory, 550 West 120th Street, MC 5247, New York, NY 10027, USA*

²*Department of Astronomy, Columbia University, 550 West 120th Street, MC 5246, New York, NY 10027, USA*

³*Barnard College, Columbia University, 3009 Broadway, New York, NY 10027, USA*

ABSTRACT

The ability of primordial gas to cool in proto-galactic haloes exposed to Lyman-Werner (LW) radiation is critically dependent on the self-shielding of H_2 . We perform radiative transfer calculations of LW line photons, post-processing outputs from three-dimensional adaptive mesh refinement (AMR) simulations of haloes with $T_{\text{vir}} \gtrsim 10^4$ K at $z \sim 10$. We calculate the optically thick photodissociation rate numerically, including the effects of density, temperature, and velocity gradients in the gas, as well as line overlap and shielding of H_2 by HI, over a large number of sight-lines. In low-density regions ($n \lesssim 10^4 \text{ cm}^{-3}$) the dissociation rates exceed those obtained using most previous approximations by more than an order of magnitude; the correction is smaller at higher densities. We trace the origin of the deviations primarily to inaccuracies of (i) the most common fitting formula (Draine & Bertoldi 1996) for the suppression of the dissociation rate and (ii) estimates for the effective shielding column density from local properties of the gas. The combined effects of gas temperature and velocity gradients are comparatively less important, typically altering the spherically averaged rate only by a factor of \lesssim two. We present a simple modification to the DB96 fitting formula for the optically thick rate which improves agreement with our numerical results to within ~ 15 per cent, and can be adopted in future simulations. We find that estimates for the effective shielding column can be improved by using the local Sobolev length. Our correction to the H_2 self-shielding reduces the critical LW flux to suppress H_2 cooling in $T_{\text{vir}} \gtrsim 10^4$ K haloes by an order of magnitude; this increases the number of such haloes in which supermassive ($M \sim 10^5 M_{\odot}$) black holes may have formed.

Key words: cosmology: theory – early universe – galaxies: formation – molecular processes

1 INTRODUCTION

It has long been known that molecular hydrogen, the most efficient coolant in metal-free gas at temperatures below 10^4 K, played a key role in formation of first-generation, “Population III,” stars (see Abel & Haiman 2000 for a review). As soon as these first stars began to shine, however, they also began to destroy H_2 via dissociating (LW) photons in the range 11–13.6 eV, to which the universe is largely transparent even at early times, $z \sim 20$ –30. The nature and extent of this photodissociation feedback has important consequences for subsequent star-formation, reionization, and the formation of massive black holes at early times.

In regions where large H_2 column densities build up ($N_{\text{H}_2} \gtrsim 10^{14} \text{ cm}^{-2}$), photodissociation is suppressed as

the LW bands become optically thick; the cooling properties of UV-irradiated primordial gas thus depend largely on its ability to “self-shield.” Unfortunately, the problem of modeling self-shielding exactly in existing studies remains intractable; in particular, approximate treatments are necessitated by two main challenges, which are the focus of this paper. First, the computational expense for three-dimensional simulations of finding the exact self-shielding column density in a large number of directions is prohibitive. As a result, studies have typically either adopted the optically-thin dissociation rate throughout (Machacek et al. 2001, 2003; Mesinger et al. 2006, 2009; Wise & Abel 2007, 2008a,b; Greif et al. 2010), relied upon estimating N_{H_2} from local properties of the gas (Bromm & Loeb 2003; Johnson et al. 2008; Gnedin et al. 2009; Shang et al. 2010; Johnson et al. 2011), or sacrificed angular resolution, finding the exact column density in a small number of directions to estimate the dissoci-

* E-mail: jemma@astro.columbia.edu; zoltan@astro.columbia.edu; gbryan@astro.columbia.edu

ation rate (Yoshida et al. 2003, 2007; Glover & Mac Low 2007a,b). Alternatively, some have employed a local method, which allows for contributions to shielding only from gas within a single smooth-particle-hydrodynamics (SPH) smoothing length (Glover et al. 2006) or within a width defined by the size of the underlying simulation grid – a method also investigated by Glover & Mac Low (2007a,b). Recently, an algorithm for finding the projected column density distribution as seen by each SPH particle, using a Healpix tessellation with 48 equal-area pixels, has been implemented by Glover & Clark (2011). In one-zone models, N_{H_2} must be specified from only “local” properties of the gas, by definition (Omukai & Nishi 1999; Omukai 2001; Omukai et al. 2008; Safranek-Shrader et al. 2010; Wolcott-Green & Haiman 2011).

Even once an estimate of the self-shielding column is obtained however, finding the exact photodissociation rate represents a large computational expense, requiring high numerical resolution in order to explicitly account for processing of the incident LW radiation as a function of frequency. Furthermore, even when only the (ortho and para) ground states of the molecule are populated, there are already a total of 76 LW transitions that contribute to the total optical depth in the relevant frequency range (photon energies below 13.6 eV). Most often, studies circumvent this difficulty by adopting analytic expressions provided by Draine & Bertoldi (1996, hereafter DB96) to model self-shielding, with a few exceptions among semi-analytic models (Haiman et al. 2000; Ciardi et al. 2000; Glover & Brand 2001, 2003) and one-dimensional simulations (Ricotti et al. 2001; Hosokawa & Inutsuka 2005, 2006), which include more detailed calculations.

The two primary goals of this study are (i) to quantify the accuracy of previous models for self-shielding, and (ii) to provide an improved analytic fit for the suppression of the photodissociation rate by shielding, which can be used in future simulations. To accomplish this, we post-process the outputs from a suite of simulations performed by Shang et al. (2010, hereafter SBH10), who studied the effects of UV-irradiation on protogalactic haloes with virial temperatures $T_{\text{vir}} \gtrsim 10^4 \text{ K}$. Within these haloes, we calculate the exact optically-thick dissociation rate at a large number of points, in a large number of directions, with a detailed treatment of radiative transfer, explicitly including the effects of density, temperature, and velocity gradients in the gas, which are most often neglected in existing models.

The rest of this paper is organized as follows. In § 2, we describe the SBH10 simulations and our methods to compute photodissociation rates with shielding. In this section, we also recapitulate several of the most common existing methods for modeling self-shielding. In § 3, we present our main results – the numerically computed suppression of the photodissociation rates. We compare these results to those obtained with each of the previously used methods, and we also elucidate the effects of gas temperature and velocity gradients, as well as the accuracy of the analytic expressions from DB96. In § 4, we discuss the implications of our results and the associated uncertainties, and we offer our conclusions in § 5.

2 NUMERICAL METHOD

2.1 Simulations

We utilize outputs from a suite of simulations performed by SBH10 with the Eulerian adaptive mesh refinement + N-body code ENZO (Bryan 1999; Norman & Bryan 1999; O’Shea et al. 2004). For the sake of brevity, we limit the discussion here to the most pertinent features of their numerical method, and refer the reader to the original study for further details.

The simulations were performed within a comoving box $1 h^{-1} \text{ Mpc}$ on a side and assuming a ΛCDM cosmological model with standard concordance parameters: $\Omega_{\text{DM}} = 0.233$, $\Omega_b = 0.0462$, $\Omega_\Lambda = 0.721$, $\sigma_8 = 0.817$, $n_s = 0.96$, and $h = 0.701$. A preliminary run was initialized with a root grid of 128^3 and no nested grids. This was performed (with radiative cooling turned off) in order to identify haloes with virial masses of a few $\times 10^7 M_\odot$ at $z \sim 10$. Three of these halo were then re-simulated at high resolution with new initial conditions – three nested grids with an effective innermost resolution of 1024^3 – and with levels of refinement added adaptively. Refinement was increased when the baryon or dark matter mass exceeded thresholds of 68 and $683 M_\odot$ respectively, and in order to maintain sufficient resolution of the local Jeans length – at least four grid cells – to prevent artificial fragmentation. Throughout, the dark matter (DM) gravity was smoothed on a scale of $0.954 h^{-1}$ (comoving) parsec. Each simulation was stopped after reaching a refinement level of 18 – a resolution of $0.0298 h^{-1}$ parsec (comoving) or 800 AU (physical).

The non-equilibrium chemistry for a gas of primordial composition was followed with a chemical network comprising 28 gas-phase reactions, including H_2 photodissociation. Radiative cooling by H_2 was modeled with the function provided by Galli & Palla (1998). Each halo was run with varied LW backgrounds in a range of intensities $J_{21} = 1 - 10^5$, where the standard normalization is implied here and throughout, $J_{\text{LW}} = J_{21} \times 10^{-21} \text{ erg s}^{-1} \text{ cm}^{-2} \text{ sr}^{-1} \text{ Hz}^{-1}$, and J_{LW} is the flux intensity at the average LW frequency ($h\nu = 12.4 \text{ eV}$). The photo-dissociating source was modeled as a blackbody with a temperature of 10^4 or 10^5 K (referred to as T4 and T5 respectively). Since in the T4 case, the photodissociation of H^- , rather than direct H_2 dissociation, controls the H_2 chemistry, we restrict our analysis here to the T5 runs. We defer further details of the adopted self-shielding model to § 2.3.

2.2 Numerical self-shielding calculations in 3D

From the simulation outputs, we selected five snapshots spanning a range in redshift $z \sim 8 - 12$, in which the gas is optically thick to LW photons. Three of these – outputs 1, 2, and 5 – are designated “cold,” as they were subjected to a modest dissociating flux, and thus have experienced significant H_2 -cooling. In outputs 3 and 4 the gas remains hot, with temperatures $\gtrsim 7000 \text{ K}$, having been exposed to a very strong LW flux that kept the gas H_2 -poor. The physical properties of the five halo snapshots are summarized in Table 1, and the radial profiles of the density, temperature, H_2 fraction, and the electron fraction are shown for each snapshot in Figure 1. We selected ~ 100 points from the cold halo

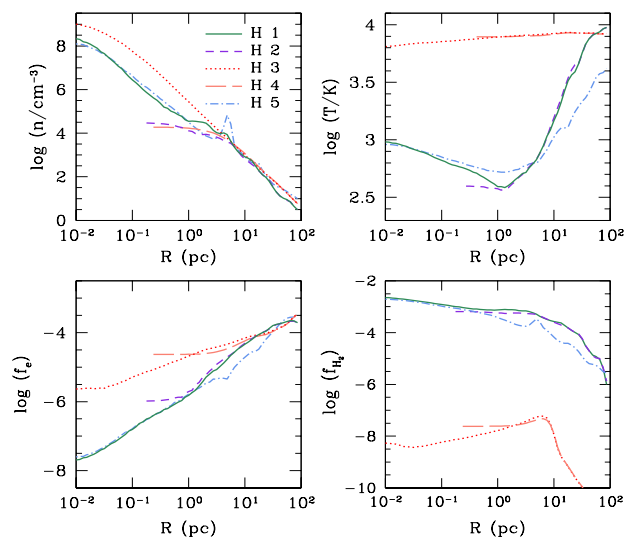


Figure 1. Spherically averaged profiles of temperature, H₂ fraction, electron fraction, and particle density in the selected simulation outputs. The radius, R , is measured from the densest point in the halo.

Table 1. Physical properties of haloes selected from the SBH10 suite of simulations. Throughout, the outputs will be referenced by number; 1-4 correspond to “Halo A” in SBH10, and #5 to “Halo C.” The redshift (z) of each output is given, along with the virial mass at the collapse redshift ($m_{\text{vir,col}}$; as in SBH10, the virial mass is defined as the total mass in baryons and dark matter within a spherically averaged overdensity of 200 with respect to the critical density). The temperature and total particle densities, T_0 and n_0 , respectively, are specified at the densest point in the halo. The intensity of incident Lyman–Werner radiation, J_{LW} , in each run is parametrized in the standard manner: $J_{\text{LW}} = J_{21} \times 10^{-21} \text{ erg s}^{-1} \text{ cm}^{-2} \text{ Hz}^{-1} \text{ sr}^{-1}$.

output	J_{21}	z	$m_{\text{vir,col}}(M_{\odot})$	$T_0(\text{K})$	$n_0(\text{cm}^{-3})$
1	10 ²	12.274	2.45×10^7	9.2×10^2	3.1×10^8
2	10 ²	12.285	2.45×10^7	4.0×10^2	3×10^4
3	10 ⁵	9.93	5.49×10^7	6.3×10^3	1.4×10^9
4	10 ⁵	9.94	5.49×10^7	7.8×10^3	1.9×10^4
5	10 ²	8.3	7.89×10^7	9.3×10^2	1.6×10^8

outputs at which to calculate the three-dimensional H₂-dissociation rate. Fewer points (~ 30) from the “hot halo” outputs were analyzed, as these are considerably more homogeneous with respect to temperature, density, and chemical composition (and are nearly optically thin even in the most dense regions). The selected points span a range in radii from 0.1 – 10 pc (physical) where the radius is defined, here and throughout, as the distance from the densest point in the halo. The number density and temperature at the selected points vary between $10 - 10^6 \text{ cm}^{-3}$ and $300 - 10^4 \text{ K}$, respectively.

2.2.1 Rate of photodissociation

H₂ is photodissociated primarily via the two-step Solomon process (Solomon 1965; see also Field et al. 1966; Stecher & Williams 1967), in which molecules are ex-

cited from the electronic ground state, $X^1\Sigma_g^+$, to the $B^1\Sigma_u^+$ or $C^1\Pi_u$ state¹, the Lyman and Werner bands respectively. Subsequent decays lead to the vibrational continuum of the ground state, rather than to a bound state ~ 15 per cent of the time, thus dissociating the nuclei.

The “pumping rate” from a given rovibrational state (v, J) to the excited electronic state with (v', J') is:

$$\zeta_{v,J,v',J'} = \int_{\nu_{th}}^{\infty} 4\pi\sigma_{\nu} \frac{J_{\nu}}{h_{\text{P}}\nu} d\nu, \quad (1)$$

where σ_{ν} is the frequency dependent cross-section and h_{P} is Planck’s constant. The frequency threshold, ν_{th} , corresponds to the lowest energy photons capable of efficiently dissociating H₂, with $h\nu \approx 11.1 \text{ eV}$. We do not include flux at $h\nu \geq 13.6 \text{ eV}$, as photons with energies above the Lyman limit are assumed to have already been absorbed by the neutral HI in the intergalactic medium (IGM) outside the halo (and were not included in SBH10).

The dissociation rate from the initial (v, J) is then obtained from the product of the pumping rate and the fraction of decays leading to the vibrational continuum from (v', J') , with a sum taken over all possible upper states:

$$k_{\text{diss},v,J} = \sum_{v',J'} \zeta_{v,J,v',J'} f_{\text{diss},v',J'}. \quad (2)$$

The dissociation probabilities here, $f_{\text{diss},v',J'}$, are obtained from Abgrall et al. (2000). The sum over rates from all lower levels, weighted by the fraction of molecules initially in each, $f_{v,J}$, then gives the total rate:

$$k_{\text{diss}} = \sum_{v,J} k_{\text{diss},v,J} f_{v,J}, \quad (3)$$

where the $f_{v,J}$ are given according to a Boltzmann distribution, unless otherwise specified.

2.2.2 Radiative transfer in the haloes

In the three-dimensional calculations of k_{diss} , the first step is to generate a set of rays² emanating from each point where the dissociation rate is to be found. These sample evenly in the azimuthal angle and in the cosine of the polar angle, tiling a sphere of radius $\sim 100 \text{ pc}$. Along each ray the properties of the gas are sampled at intervals determined by the size of the underlying grids; the distance between sample points is typically 0.01 pc in regions with the highest levels of refinement, and increases to $\sim 5 \text{ pc}$ toward the outskirts (areas with lowest resolution) of the halo.

In our fiducial calculations, the spectrum of the incident radiation is initialized to be flat in the range 11.1–13.6 eV, with the implicit assumption that processing of the LW background in the IGM is negligible. Note that, in general, the cosmological background *will* be modified, though primarily by HI absorption, and not by H₂ itself (Haiman et al. 2000, hereafter HAR00, see also Ricotti et al. 2001) and the impact of the resulting “sawtooth” modulation is considered

¹ $C^1\Pi_u$ is split into Π_u^+ and Π_u^- states owing to Λ -doubling, the two-fold degeneracy of each rotational level (J).

² We use the analysis toolkit ΥT (Turk et al. 2010) to interface with the raw simulation data; see § 3.5 for the required angular resolution.

in § 4.2. Tracing a ray from the outside in, the gas is treated as a series of thin slabs, each with uniform density, temperature, bulk velocity, and chemical composition defined at the sample point; the column density is specified by $n_{\text{H}_2} \times \Delta s$, where Δs is the width of the slab. The frequency-dependent optical depth, τ_ν , of the slab is then obtained by summing over contributions from all included LW transitions, each of which is modeled by a Voigt profile. The rest-frame frequencies are Doppler shifted according to the slab’s line-of-sight velocity relative to the point where the dissociation rate is to be calculated. The numerical wavelength resolution ($\Delta\lambda = 2 \times 10^{-4} \text{ \AA}$ at the lowest temperatures) is set adaptively in order to always resolve the thermal line width and is sufficient to explicitly account for overlap of the Lorentz wings. The necessary molecular data for these calculations are provided by Abgrall et al. (1993a,b).

We include transitions from the 29 bound rotational levels within the ground electronic and vibrational ($v = 0$) states to excited states with $v' \leq 37$, $J \leq 10$; in total, this amounts to 1492 possible transitions out of $v = 0$. We do not include absorption from higher vibrational levels, which are populated only at particle densities much larger than we consider here, $n \gtrsim 10^8 \text{ cm}^{-3}$ (Le Bourlot et al. 1999, hereafter LPF99, Flower & Harris 2007). In our fiducial calculations, the rotational levels of $v = 0$ are populated according to a Boltzmann distribution defined by the temperature of the slab, irrespective of the local density. Strictly speaking, populations in rotational states within $v = 0$ do not thermalize until (temperature dependent) critical densities are reached, usually taken to be $n_{\text{crit}} \simeq 10^4 \text{ cm}^{-3}$ (but see Table 1 in Flower & Harris 2007), at which depopulation of excited states is dominated by collisional de-excitation.³ To further address this issue, we perform an additional set of calculations in which all molecules are assumed to be in the ground states of para (ortho) hydrogen, $v = 0$, $J = 0$ (1). In this case, all 76 possible transitions are included; the results are discussed in § 4.4.

Finally, having found τ_ν along a sightline, the photodissociation rate is calculated at the point of interest. This procedure is repeated for each of the sight lines and the final rate is obtained from a simple average over all directions. Note, however, that the spherical average is only meaningful in the case of an isotropic UV background. This would be relevant when the Olber’s integral for the local flux is dominated by a large number of distant sources. For haloes with unusually bright and close neighbors, the flux can be dominated by a single (or a few) of the nearby sources. In § 4.3 we discuss a radiation field with a preferential direction that would be relevant in this case, and interpret our results in this context.

One remaining caveat is the possibility of H_2 shielding by HI. In general, Lyman-series absorption within the haloes can suppress the H_2 dissociation rate by a large factor, though this requires high optical depth in the wings of the HI lines, and thus $N_{\text{HI}} \gtrsim 10^{22} \text{ cm}^{-2}$ (Wolcott-Green & Haiman 2011). Sufficiently large neutral column densities are indeed present in the the outputs we analyze, though only at small

³ Note that the critical density is different for each species that perturbs the molecule; here and throughout, we refer to n_{crit} for collisions with atomic hydrogen only.

radii (\lesssim a few pc), and the resulting modification of k_{diss} in these regions is discussed in § 4.2.

2.3 Approximate treatments of self-shielding

Approximations for self-shielding in existing simulations have been necessitated by the two challenges mentioned above: first, the computational expense for simulations of finding the H_2 column density in a large number of directions is prohibitive. An estimate for this inherently non-local quantity therefore typically must be obtained from purely local information. In § 2.3.1, we give a detailed account of several ways in which this is commonly achieved. Second, calculating the exact suppression of the optically-thin rate, with full radiative transfer in each LW line, is expensive, requiring high numerical wavelength resolution, as well as the inclusion of non-local effects from the temperature and velocity structure in the gas. Therefore, studies often rely on an analytic expression for the optically-thick rate provided by DB96. We briefly describe this method in § 2.3.2, including the assumptions and limitations in applicability of the analytic fitting formula.

2.3.1 The self-shielding column density

In order to estimate the column density, several common methods make use of local properties of the gas to define a characteristic length scale, L_{char} ; the column density is then obtained from:

$$N_{\text{H}_2} = n_{\text{H}_2} L_{\text{char}}, \quad (4)$$

with the implicit assumption that the H_2 number density, n_{H_2} , is constant at the local value over the length L_{char} . Several methods have been used to define a characteristic length scale:

The Jeans Length

A common approach in both simulations and one-zone models is to assume the total mass in the optically-thick region is of order the Jeans mass, with L_{char} then defined using the local Jeans length. In regions where particle densities exceed $n_{\text{tot}} \gtrsim 10^5 \text{ cm}^{-3}$, SBH10 have shown that this provides a very accurate estimate of N_{H_2} ; however, in lower density regions, it typically overestimates the integrated N_{H_2} by up to an order of magnitude (see their Figure 9). This method also does not account for temperature or velocity gradients in the gas.

The Sobolev Length

Large velocity gradients will cause the LW resonances, as seen from a given point in the cloud, to appear shifted from their rest-frame wavelength, making the systematic depletion of dissociating photons less efficient than if the gas were static. If the fluid motions are largely disordered and/or supersonic, the exact column density along a line of sight can then exceed the effective self-shielding column density, N_{eff} , by a large factor.

In general, N_{eff} depends on the detailed velocity structure in the gas; however, it may be estimated by taking a characteristic length equal to the Sobolev length, L_{Sob} (Sobolev 1957). This defines a distance over which the mean

(macroscopic) fluid velocity changes by a factor of the (microscopic) thermal velocity of the molecules, v_{th} ,

$$L_{Sob} \equiv \frac{v_{th}}{|dv/ds|} \quad (5)$$

with the assumption that dv/ds is constant. Then for a given sightline, L_{Sob} is the distance at which the absorption profiles will be shifted by one local line width. In adopting the Sobolev length for L_{char} , it is implicitly assumed that Doppler shifts in the LW resonances of molecules closer than L_{Sob} can be ignored, and that all molecules beyond this distance contribute negligibly to shielding.

Strictly speaking, this method should only provide an accurate estimate of N_{eff} if the velocity gradient is both large and monotonic and the intrinsic line widths are negligible in comparison to the Doppler cores. If instead the Lorentz wings (and line overlap) become important, these will render the Doppler shifts irrelevant and this method will underestimate self-shielding as a result. None the less, it may prove useful, particularly if motions of the fluid are supersonically turbulent. In fact, a similar method has been fruitfully employed in the analogous case of the escape fraction of photons from dense, metal-free gas (e.g. Yoshida et al. 2006).

In order to generalize to a non-spherically symmetric geometry, one option is to define a single L_{Sob} from the mean Sobolev length over all directions, which we will refer to as L_{Sob}^s . Alternatively, in direct analogy with the three-dimensional self-shielding calculation, we could find L_{Sob} and the corresponding dissociation rate for each sightline and take the mean rate over all directions (hereafter L_{Sob}^k). Clearly, this approach should provide a reasonably accurate estimate of the dissociation rate if the corresponding column density is a good approximation for N_{eff} along every direction. Finally, we could take the minimum Sobolev length (L_{Sob}^{min}), or an average column density (L_{Sob}^N), over all directions.

A ‘‘Sobolev-Like’’ Length

A method akin to the Sobolev length has been recently employed and shown to provide a fairly accurate estimate of the integrated column density by Gnedin et al. (2009), though in a different context than that of the present work (they model self-shielding in individual star-forming regions of a Milky Way progenitor). In this case, a characteristic length is obtained from

$$L'_{Sob} \equiv \frac{\rho}{|\nabla\rho|}, \quad (6)$$

thereby defining a distance over which the gas density, ρ , should be significantly diminished, and assuming that the optical depth beyond L'_{Sob} is negligible.

We expect this method to prove most useful when the length scale of significant decrease in the gas density is shorter than those over which large variations in the H₂ fraction or the gas velocity occur. Note that the aim is to define a distance beyond which the gas contributes negligibly to shielding, so extrapolation along lines of sight for which $d\rho/ds > 0$ is not meaningful (this happens for off-centre points, in directions toward the halo centre). Thus, we define L'_{Sob} , L'_{Sob}^k , and L'_{Sob}^N in a similar manner as described above for the traditional Sobolev-like length, but include in the averaging only those sight-lines for which $d\rho/ds < 0$.

The ‘‘Six-Ray Approximation’’

Finally we consider one non-local method, variations of which have been implemented in simulations by, e.g., Yoshida et al. (2003, 2007) and Glover & Mac Low (2007a,b). In this case, the exact N_{H_2} is obtained by integrating the H₂ profile along six lines of sight parallel to the Cartesian axes. The value of the shield factor for each is obtained from one of the DB96 fits (equations 8 or 9 below) and the final rate is found by averaging over six directions.⁴ In spite of the low angular resolution, this approach is expected to be reasonably accurate unless the gas is (supersonically) turbulent, in which case neglecting Doppler shifts of the LW lines will likely cause the integrated N_{H_2} to substantially exceed the effective self-shielding column density.

2.3.2 Analytic approximations for the photodissociation rate

Self-shielding by H₂ has received attention over the years for its importance in the context of interstellar clouds (e.g. Hollenbach et al. 1971; Shull 1978; Federman et al. 1979; de Jong et al. 1980; Abgrall et al. 1992; Heck et al. 1992; Le Bourlot et al. 1993; DB96). A number of analytic models for the attenuation of the incident flux have been put forward, as explicit calculations of the radiation field as a function of both cloud depth and frequency have not previously been feasible. In the last decade, however, studies have most often employed the expressions provided by DB96. These authors model a semi-infinite, static slab of gas irradiated on one surface, and parametrize the dissociation rate with a ‘‘shield factor’’ as:

$$k_{diss}(N_{H_2}, T) = f_{sh}(N_{H_2}, T) \times k_{diss}(N_{H_2} = 0, T), \quad (7)$$

where $k_{diss}(N_{H_2} = 0)$ is the optically-thin rate. They show that, at low temperatures ($T \sim$ a few $\times 10^2$ K), suppression of the optically-thin rate can be well approximated by a simple power-law that depends only on the H₂ column density as:

$$f_{sh,36}(N_{H_2}) = \min \left[1, \left(\frac{N_{H_2}}{10^{14} \text{ cm}^{-2}} \right)^{-3/4} \right]. \quad (8)$$

These authors also provide a slightly more complicated functional form, which attempts to incorporate a temperature dependence due to thermal broadening of the lines, and which fits their results more accurately:

$$f_{sh,37}(N_{H_2}, T) = \frac{0.965}{(1 + x/b_5)^2} + \frac{0.035}{(1 + x)^{0.5}} \times \exp[-8.5 \times 10^{-4} (1 + x)^{0.5}]. \quad (9)$$

Here $x \equiv N_{H_2}/5 \times 10^{14} \text{ cm}^{-2}$, $b_5 \equiv b/10^5 \text{ cm s}^{-1}$, and b is the Doppler broadening parameter (equations 8 and 9 are given in DB96 as their equations 36 and 37, respectively, as indicated by the subscripts). Because 9 is the more accurate of the two, this will be the focus of our discussion henceforth.

These expressions have been ubiquitously used to model self-shielding in simulations. While it is often noted that

⁴ Note that Yoshida et al. (2003) use instead the shield factor calculated for the line of sight with minimum H₂ column density.

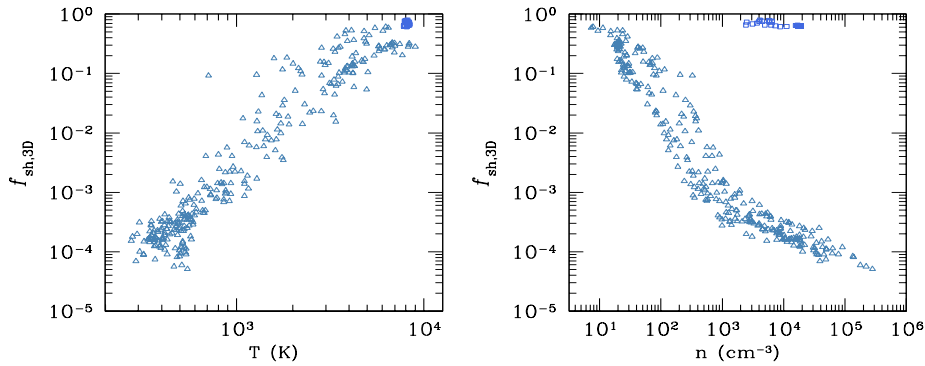


Figure 2. The numerical results for the shield factor in three–dimensions, $f_{\text{sh},3\text{D}}$, are shown at the local temperature (left–hand panel) and particle density (right–hand panel). Points are included from all five halo outputs; those from cold and hot haloes are denoted (here and in all subsequent figures) by open triangles and squares, respectively.

they are only strictly valid in the static limit, it should be emphasized that DB96 make several assumptions in their modeling which limits the applicability of the expressions they derived. Most importantly, they consider a *cold* gas, with $T \lesssim$ a few $\times 10^2$ K. Furthermore, they assume either (i) a steady–state rovibrational distribution that includes absorptions from $v > 0$ or (ii) an isothermal gas with H_2 level populations given by a Boltzmann distribution. Also included are shielding by dust and the formation of H_2 on grains. None the less, their fitting formulae are often implemented in contexts quite different from the original study, in which these assumptions are not well motivated. In light of this, § 3 addresses the accuracy of equation (9) in the present context, i.e. for metal–free gas with a wide range of densities $10 \lesssim n_{\text{tot}} \lesssim 10^6 \text{ cm}^{-3}$ and temperatures $300 \lesssim T \lesssim 10^4 \text{ K}$, and in which dust, as well as UV–pumping from excited vibrational states is likely negligible (see § 4.4).

3 RESULTS

The numerical results for the photodissociation rate in three–dimensions, parametrized (as above) by a shield factor, $f_{\text{sh},3\text{D}}$, are shown in Figure 2 as a function of the local temperature and particle density of each point. The trend toward decreased optical depth at high temperatures and low densities is due to the characteristic structure in these haloes, in which regions farther from the dense core are both hotter and more rarefied, and typically see lower shielding columns (see Figure 1). The exception is the hot haloes, in which the gas remains optically thin even at small radii, where $n \gtrsim 10^{3-4} \text{ cm}^{-3}$, due to the low molecular fraction. As a result, these hot haloes (outputs 3 and 4) will not be further addressed in great detail, as they add little to the discussion of self–shielding.

Figure 3 shows these results in comparison with several approximate methods. The four panels show f_{sh} given by equation (9), and in each, the column density is specified by one of the methods discussed in § 2.3.1. Because studies typically must employ estimates for N_{H_2} as well as an analytic fit for the shield factor, the overall discrepancies seen here are representative of what would be realized in a simulation.

A clear trend is immediately apparent in Figure 3,

which appears independent of how the column density is estimated: all approximate methods significantly overestimate shielding compared to our numerical results in the range $10^{-3} \lesssim f_{\text{sh},3\text{D}} \lesssim 0.3$, while each is considerably more accurate at smaller values of $f_{\text{sh},3\text{D}}$. In principle, this discrepancy may arise from physical effects, i.e. Doppler shifts in the LW absorption lines, causing self–shielding to be weaker than in a static gas, or variations in the gas temperature, resulting in depopulation of states that contribute most to dissociation. Alternatively, it may be due to inaccuracy of the analytic fit for the f_{sh} itself. In what follows, we examine each of these possibilities in turn, to determine how much each effect contributes to the observed trend.

3.1 Analytic approximations for f_{sh}

The left panel of Figure 4 shows a comparison of the shield factor obtained from the DB96 expression (equation 9), against the results from our numerical calculations at $T = 500, 1000,$ and 5000 K . In the latter, the gas is modeled as a static and isothermal slab, in order to isolate the accuracy of equation (9) from the effects of temperature and velocity gradients. It is apparent from this figure that the trend of discrepancies seen in all four panels of Figure 3 is caused in large part by the inaccuracy of the fitting formula itself at temperatures greater than a few hundred Kelvin. (Note that, as shown in Figure 2, all points in the simulation with $f_{\text{sh},3\text{D}} \gtrsim 10^{-3}$, which are discrepant, are at $T > 500 \text{ K}$.)

We have found that the large discrepancies – equation (9) underestimates the numerical results by up to an order of magnitude – are due to the temperature dependence of f_{sh} for thermalized H_2 populations. To illustrate this, consider a gas in local thermodynamic equilibrium (LTE) at a (uniform) temperature of a few hundred Kelvin, so that only the lowest rotational states within the vibrational ground state will be significantly populated (for reference, the energies of the $v = 0, J = 1, 2$ states are $\approx 170, 509 \text{ K}$). As the temperature is increased, the populations will be diluted over a greater number of rotational levels (e.g. at $T \sim$ several thousand Kelvin, non–negligible populations build up in $J \lesssim 15$). The upshot of thus spreading absorbers over a

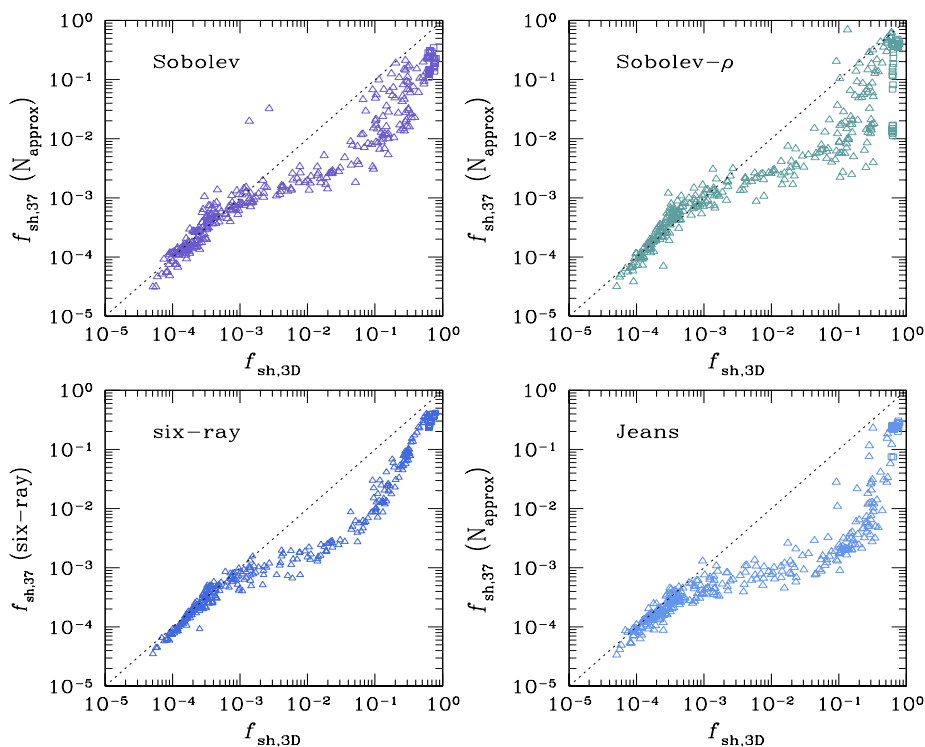


Figure 3. Comparison of our numerical results for the average shield factor in three dimensions, $f_{\text{sh},3\text{D}}$, with those given by the analytic fitting formula ($f_{\text{sh},37}$ in equation (9), taken from DB96). Clockwise from the upper left, the column density is specified by the best-fitting Sobolev and Sobolev-like (“Sobolev- ρ ”) methods, (L_{Sob}^k and L'_{Sob} respectively; see § 2.3.1), and the Jeans length. The lower left panel shows results of the only previous non-local approach, the “six-ray method,” in which equation (9) is used to calculate the shield factor along six sight lines, and an average over these gives $f_{\text{sh},37}(\text{six-ray})$. Non-local effects of velocity and temperature gradients are included in the calculation of $f_{\text{sh},3\text{D}}$, as described in § 2.2.

greater number of states is that shielding becomes weaker⁵. This effect is not modeled by the DB96 expression (equation 9), which accounts only for decreased shielding due to thermal broadening of the lines. As a result, we find that it is accurate only for a rotationally-cold gas, i.e. when molecules occupy only the first few J states (we show this explicitly in Figure 11).

The inaccuracy of this analytic fit at high temperatures has been noted previously by Ahn & Shapiro (2007), who proposed that it may be remedied by artificially increasing the thermal broadening parameter used in equation (9). We have found that this method yields very little improvement in accuracy; however, a much better fit to our numerical results is obtained with only a slight modification of equation (9) as follows. We treat α , below, as a free parameter, where $\alpha = 2$ in the original expression:

$$f_{\text{sh}}(N_{\text{H}_2}, T) = \frac{0.965}{(1 + x/b_5)^\alpha} + \frac{0.035}{(1 + x)^{0.5}} \times \exp[-8.5 \times 10^{-4} (1 + x)^{0.5}]. \quad (10)$$

We find that $\alpha = 1.1$ improves the fit drastically in the

high temperature regime, with little accuracy sacrificed at low temperatures. Physically, this result makes sense, since reducing α weakens the temperature effect, which, as we argued, is overestimated in the original equation. The modified expression agrees with the numerical results to within a factor of two at $500 < T < 5000$ K, and $N_{\text{H}_2} \leq 10^{20} \text{ cm}^{-2}$, as shown by the solid curves in Figure 4. Furthermore, as the figure shows, the largest discrepancies occur (a) at low temperature, $T = 500$ K, and larger values of the shield factor, $f_{\text{sh}} \gtrsim 10^{-2}$, or (b) high temperature, $T \gtrsim 5000$ K and $f_{\text{sh}} \lesssim 10^{-3}$. In the context of our study, these combinations are, in fact, never physically realized, as low temperatures ($T \approx 500$ K) are only reached via H_2 radiative cooling, implying that in cold gas, large column densities will have built up and the shield factor will be small; for the same reason, the gas cannot remain hot once it has become strongly self-shielding (see the temperature and density profiles in Figure 1). Overall, we find that the agreement between equation (10), with $\alpha = 1.1$, and the results for $f_{\text{sh},3\text{D}}$ in the haloes is ≈ 15 per cent.

3.2 Impact of velocity gradients

As previously described, the existence of internal velocity gradients will cause a given parcel of gas to see more flux than it would in a static gas, owing to Doppler shifts of the LW resonances in regions of the fluid moving at large

⁵ The importance of diluting the populations over higher energy states was pointed out by Federman et al. (1979), who showed that for a thermal distribution, including absorption from $J = 2$ changed their results by ~ 40 per cent compared to those in ortho and para ground states were populated.

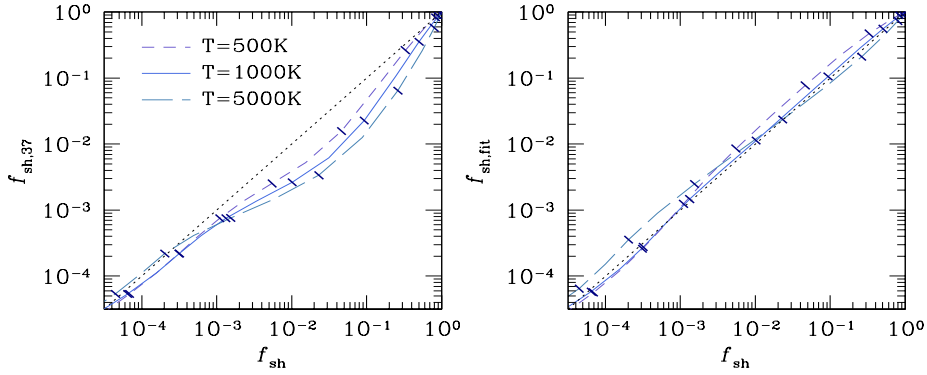


Figure 4. The results from equations (9; left panel) and (10, with $\alpha = 1.1$; right panel) are compared against the numerical results for f_{sh} at $T = 500, 1000,$ and 5000K . In the latter, the gas is treated as an isothermal and static slab, irradiated uniformly on one side. Tick marks along each curve indicate ten-fold decreases (left to right) in the column density, with $N_{\text{H}_2} = 10^{20} \text{ cm}^{-2}$ at the lower left; the dotted curves are 45-degree lines for reference.

relative velocities. This can lead the actual N_{H_2} to exceed the effective column density by a large factor, and could thus also contribute to $f_{\text{sh}}(N_{\text{approx}})$ overestimating shielding compared to the numerical results (see Figure 3).

To quantify the magnitude of this effect, we repeated our three-dimensional calculations with gas velocities artificially set to zero everywhere. The results, shown in the left panel of Figure 5, can be divided roughly into three regimes: strongest, intermediate, and weakest shielding; the transition between the first (latter) two occurring at $f_{\text{sh},3\text{D}} \simeq 4 \times 10^{-4} (2 \times 10^{-2})$. The dissociation rate is increased in the non-static case by an average of 6, 65, and 20 per cent, respectively, in the three regimes (though in the intermediate case, certain points see dissociation rates that are factors of up to 4-5 times greater due to relative gas velocities).

In order to understand why this effect operates differently in the three regimes, let us first consider points where shielding is weakest, $f_{\text{sh},3\text{D}} \gtrsim 2 \times 10^{-2}$. In Figure 6, the shield factors are shown for individual sight lines emanating from a single point in this regime; these are shown for both the static and non-static cases (closed and open triangles, respectively) at the integrated N_{H_2} in each direction. In the lower panel, the relative line of sight velocities along all 16 directions are shown. Three directions are distinct from the rest, in that they see the largest velocities as well as the greatest integrated column densities – the three bottom curves in the lower panel correspond to the three right-most points in the upper panel. This highlights an important point about the dynamics in these simulations: a coherent flow of the fluid onto the densest region dominates the gas velocities, rather than turbulence. Thus, large frequency shifts in the H_2 lines occur only along sight lines aligned with this flow, and while they clearly do change the dissociation rate in these directions, variations in these smallest values of the shield factor have little effect on the spherically averaged value. In the strongest shielding regime, the column densities are sufficiently high that large damping wings of the lines render frequency shifts irrelevant. We have verified this by artificially decreasing the column density of each slab along these sightlines by a factor of 100 and repeating the full calculations with velocities both on and off; in this test, $f_{\text{sh},3\text{D}}$ becomes several times larger in the non-static case.

In the intermediate regime, the damping wings of the lines are not significant, and frequency shifts have a larger impact on the dissociation rate as a result. This is *not*, however, because the total column densities are lower than in the previous case. The integrated N_{H_2} 's along sight lines emanating from these points are, in fact, comparable to those in the strongest shielding regime, but the points themselves are in regions with much higher temperatures (i.e. $T \gtrsim 10^3\text{K}$, compared to a few hundred Kelvin; see Figure 2). This highlights the importance of coupling between the effects of temperature and velocity gradients. As previously discussed, increased temperature dilutes the H_2 populations over a greater number of rovibrational levels; the upshot here is that diminished Lorentz wings of transitions originating from these no longer cancel the effects of Doppler shifts. In other words, the column density in a given rovibrational level *is* smaller than in the strongest shielding regime, though the total N_{H_2} for individual sight lines is comparable.

3.3 Impact of temperature gradients

While not as often addressed as the effect of frequency shifts, variations in the gas temperature along a given line of sight may also significantly alter the self-shielding behaviour, particularly for a gas in LTE. There are two distinct temperature-induced effects: (i) changes in the level populations (specific to the LTE case), and (ii) changes in the widths of individual lines.

Consider the population effect first. For a given parcel of gas with temperature T_0 , along a given direction, deviations in the temperature from T_0 and the resulting change in the rotational distribution may either increase or decrease the populations of the levels from which most dissociating transitions originate. In general, if (a) T_0 is small (\sim a few $\times 100\text{K}$) and the temperature is increased along a sightline, or (b) the *difference* between the temperature of the shielding gas and T_0 is very large, the result is to depopulate the states from which most UV-pumping occurs, and thus to decrease the effective column density. On the other hand, if the temperature variations along a sightline are not large, the shielding may be increased compared to the isothermal case, owing to boosted populations in states from which the

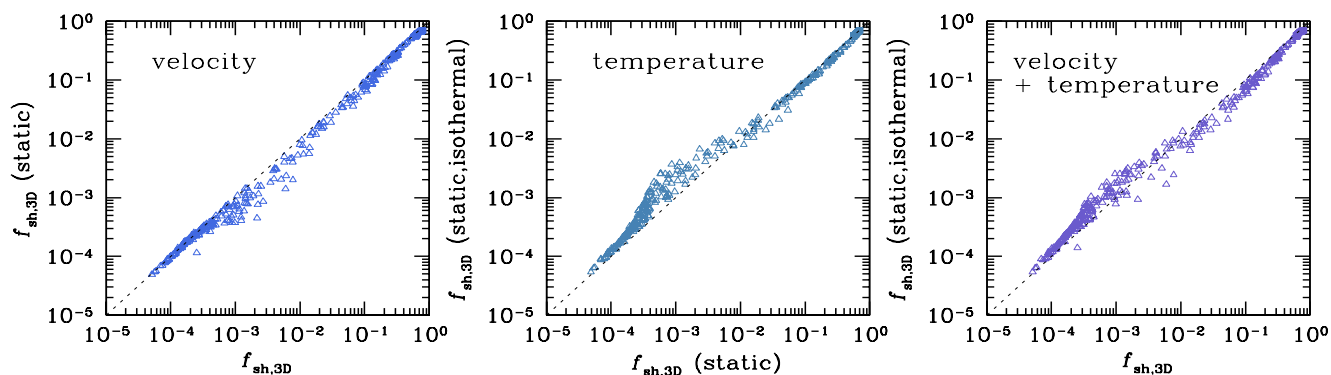


Figure 5. *Left-hand panel:* the fiducial numerical results, $f_{\text{sh},3\text{D}}$, are compared to those in which the gas is assumed to be static. *Middle panel:* isolates the effect of setting the temperature constant along each sightline (with the gas again assumed to be static along both axes). *Right-hand panel:* shows the combined effect of the velocity and temperature variations, by comparing the fiducial results with those in which the gas is assumed to be both isothermal and static. Note that, here, “isothermal” does not imply that temperature is the same for all points, but rather that $T = T_0$ along all sight lines, where T_0 is the temperature where the dissociation rate is calculated.

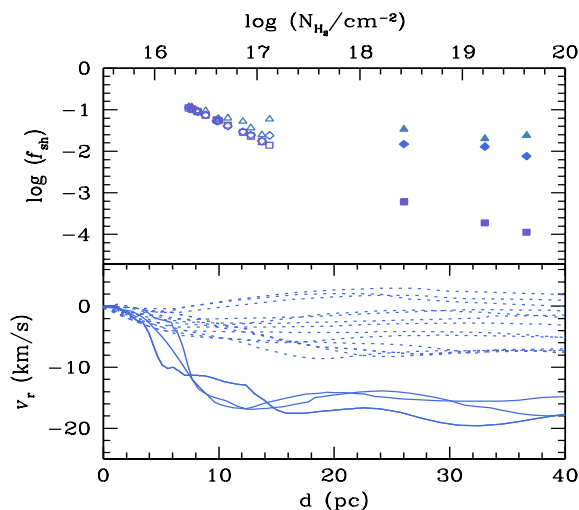


Figure 6. *Upper panel:* comparison of the numerically-calculated shield factors along individual sight lines from a single point (triangles) with those obtained when the gas is assumed to be static (diamonds) or both static and isothermal (squares). The full spherically averaged photodissociation rate is increased 23 per cent (30 per cent) compared to the static (static and isothermal) case. *Lower panel:* relative line of sight velocities along the same directions as shown in the upper panel. The three lower (solid) curves correspond to the three sight lines with largest total N_{H_2} (closed symbols) in the upper panel.

strongest transitions (i.e. those for which the product of the oscillator factor and dissociation probability is largest) originate.

Interestingly, we find that the line-width effect may be equally or more important than the above population-induced changes. Consider again our gas parcel with temperature T_0 , shielded, for simplicity, by a single slab of gas at $T < T_0$. The narrowed thermal widths of absorption lines in the slab result in overall much weaker shielding, in comparison to the isothermal case (though the opacity at the line centre is actually increased). Furthermore, because this effect may act in the same direction as the population-induced

changes, shielding can be greatly reduced for the case in which $T < T_0$. This is illustrated in Figure 6, in which the open squares show the results when both the velocity and temperature are held constant along all sight lines. Recall that these sight lines emanate from a point which lies in the weakest shielding regime; the temperature is $\sim 3500\text{K}$ where the dissociation rate is calculated, while along the rays passing through the dense central core of the halo (for which N_{H_2} is largest), the temperature drops as low as 300–400K. The resulting narrowing of the thermal cores in the shielding gas, along with depopulation of excited rotational states from which a large fraction of the dissociating transitions occur, drastically reduces the effective column density and correspondingly increases f_{sh} . In principle, this effect could also contribute to the approximate methods overestimating self-shielding as compared to the numerical results; however, these changes again are typically only significant for the smallest values of the shield factor (sightlines which are directed through the dense core), and thus have a small effect on the spherically averaged value.

Finally, we consider the simplified model of a single shielding slab with $T > T_0$. In this case, the larger thermal widths in the shielding gas yield greater optical depth in the wings of the Voigt profiles of the dissociating transitions, and this can outweigh the reduced line centre opacity. This effect depends on N_{H_2} along the sightline in question, and there is a column density-dependent $T_{\text{max}} > T_0$, at which f_{sh} is a minimum, above which further increases in the temperature lead to weaker shielding. This is not important in the weakest shielding regime, as T_0 here is already very high (see Figure 2), so that few sight lines see a significant increase in the temperature. In the strongest shielding regime, the broader thermal cores are unimportant because the absorption lines already have large damping wings, so that extremely high temperatures would be required for this effect to operate. It is, however, important in the intermediate regime; as illustrated in the middle panel of Figure 5. This panel shows that shielding is always *weaker* when the temperature is held constant along sight lines for $f_{\text{sh},3\text{D}}(\text{static}) < 10^{-2}$. (Here, gas velocities have again been set to zero so as to isolate the effect of non-uniform temperature, which cou-

ples to that of velocity gradients). However, this cannot be entirely attributed to the line-width effect, as temperature changes in this regime often also induce stronger shielding owing to increased populations of important lines, as mentioned above. Interestingly, the cumulative effect counteracts that of Doppler shifts, which are also more important in this regime, with the result that “turning on” both temperature and velocity gradients causes only a small scatter around the original results, as illustrated in the right-hand panel of Figure 5.

3.4 Approximate self-shielding column densities

The only remaining source of discrepancy between the numerical and approximate results for f_{sh} are the column density approximations, N_{approx} , obtained either from local quantities, or from the six-ray method. In order to isolate the accuracy of each method described in § 2.3.1, we have calculated the dissociation rate numerically, assuming a single slab of shielding gas with $N_{\text{H}_2} = N_{\text{approx}}$. The results are compared to the exact $f_{\text{sh},3\text{D}}$, in Figure 7, and the mean errors from each method are quantified in Table 2. In the three-dimensional calculation, the gas temperature and velocity are held constant along all sightlines, so as to isolate the accuracy of each method for specifying N_{approx} ⁶.

Over the full range of radii we consider, the Sobolev length proves the most accurate purely local estimate for the effective column density. This is perhaps surprising, given the results in § 3.2, where we have shown that velocity gradients do not alter the observed LW flux within these haloes significantly. In fact, because of the unimportance of velocity gradients for our results, we might expect that the Sobolev length should not provide a meaningful length scale, L_{char} , for self-shielding. It is worth noting that this method is also the only one considered here, to the best of our knowledge, which has not been implemented in simulations in the context of self-shielding (though it is commonly used in the opposite case, to compute the escape fraction of photons traveling outward). Indeed, while it is not obvious how to justify the success of this method, its potential usefulness in simulations should be highlighted; though the scatter is larger than from the six-ray method, the computational expense is dramatically reduced.

In fact, Figure 7 shows that, for $f_{\text{sh}} \lesssim 10^{-3}$, all three local methods provide surprisingly accurate estimates of the column density, given the relatively crude assumptions made in approximating the characteristic length scale for shielding. However, while both Sobolev and Sobolev-like methods are also reasonably accurate in the less shielded regime, in agreement with SBH10, we find that the Jeans length typically underestimates the dissociation rate by an order of magnitude or more at $f_{\text{sh},3\text{D}} \gtrsim 10^{-3}$, i.e. in regions where the number density is low, $n_{\text{tot}} \lesssim 10^4 \text{ cm}^{-3}$, and temperature is high, $T \gtrsim 10^3 \text{ K}$ as shown by Figure 2 (see also Figure 9 in SBH10).

⁶ We note that it is somewhat awkward to compare the results from the Sobolev length to the numerical results assuming a static slab – formally the Sobolev length is infinite in static gas. However, Figure 7 clearly illustrates that the efficacy of this method here *cannot* be attributed to the presence of velocity gradients.

Table 2. The accuracy of each method for estimating the column density (see § 2.3) is quantified by the mean of $f_{\text{sh}}(N_{\text{approx}})/f_{\text{sh},3\text{D}}$ (isothermal, static). Ratios are reported separately for regions with particle densities above and below 10^4 cm^{-3} , corresponding roughly to a cut-off around $f_{\text{sh},3\text{D}} \approx 10^{-3}$. Numbers in parentheses indicate the 1σ scatter. Boldface values highlight the best-fitting Sobolev and Sobolev-like (L'_{Sob}) methods.

	$n < 10^4 (\text{cm}^{-3})$	$n > 10^4 (\text{cm}^{-3})$
L_{Jeans}	0.50 (0.38)	0.96 (0.17)
L_{Sob}^s	1.7 (4.3)	1.1 (0.3)
$^a. L_{\text{Sob}}^k$	1.3 (1.3)	1.0 (0.3)
L_{Sob}^N	0.48 (0.44)	0.46 (0.23)
$L_{\text{Sob}}^{\text{min}}$	6.1 (25)	2.1 (0.7)
$^b. L_{\text{Sob}}^{\prime s}$	1.4 (0.9)	1.1 (0.2)
$L_{\text{Sob}}^{\prime k}$	0.66 (0.75)	0.61 (0.14)
$L_{\text{Sob}}^{\prime N}$	0.78 (0.49)	0.67 (0.31)
$L_{\text{Sob}}^{\prime \text{min}}$	3.0 (6.5)	1.6 (0.3)
six-ray	0.93 (0.09)	0.97 (0.05)

^{a.} Recall that, in this method, the Sobolev length for each sightline is used to calculate the dissociation rate, and the final rate is obtained from a simple average over all directions.

^{b.} In this case, the rate is calculated given a single column density specified by the spherically averaged “Sobolev-like” length.

Not surprisingly, the six-ray method proves more accurate than the “local” methods. In fact, in the absence of temperature and velocity gradients, six sightlines would suffice for convergence of the spherically averaged rate. However, larger discrepancies occur if the six-ray results are compared to the full three-dimensional calculation (this comparison is not shown) rather than the static and isothermal case; this is simply because the integrated N_{H_2} is then, in general, not equal to the effective self-shielding column density. In this case, the average ratio (1σ scatter) for $f_{\text{sh}}(\text{six-ray})/f_{\text{sh},3\text{D}} = 1.2 (0.1)$ and $1.1 (0.5)$ for points with particle densities above and below 10^4 cm^{-3} , respectively (c.f. Table 2). Recall that most often this method is implemented by integrating to find the total N_{H_2} along each of the directions and plugging this into equation (8), or (9); therefore, it does not account for variations in the temperature and velocity along the rays. (An exception is the study by Yoshida et al. 2007, in which N_{H_2} is summed along each ray, excluding gas particles with relative velocities significantly larger than the local thermal velocity.)

3.5 Angular resolution for f_{sh} in 3D

In order to determine the required angular resolution for the numerical calculations, we performed a convergence test for the spherically averaged $f_{\text{sh},3\text{D}}$ using 50 points selected from the five simulation outputs, spanning the full range of radii we consider, $0.1 \lesssim R \lesssim 10 \text{ pc}$. The mean error in the shield factor, $f_{\text{sh},3\text{D}}$, for these points was found to be three (two) per cent for an increase from $16 \rightarrow 25$ sightlines ($25 \rightarrow 49$).

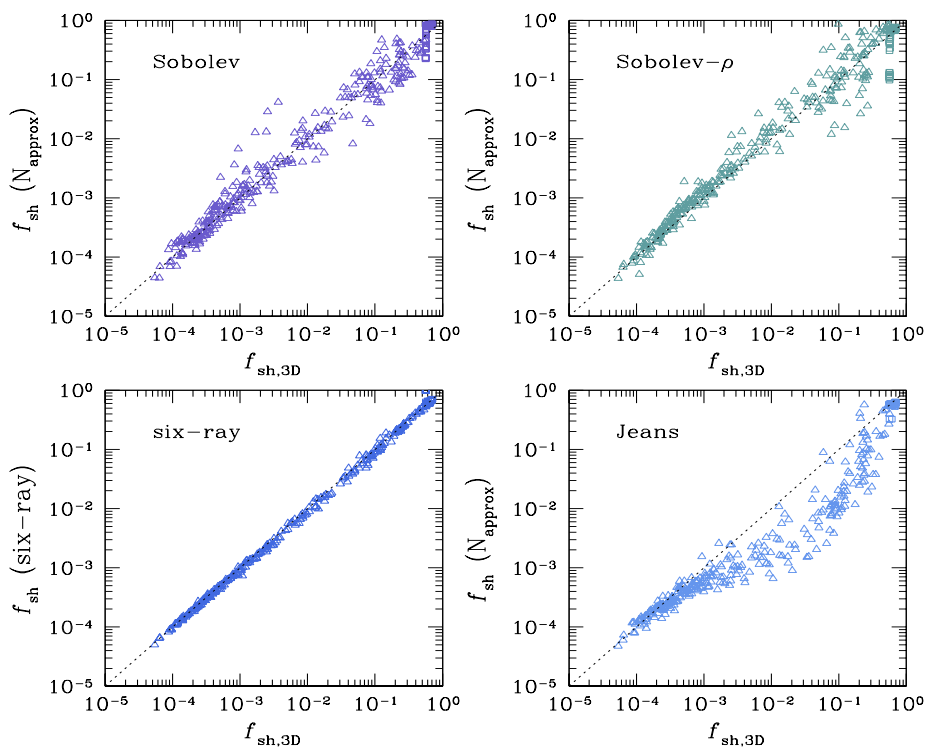


Figure 7. Comparison of the numerical results for the shield factor in three dimensions, $f_{\text{sh},3\text{D}}$ to those obtained from a single slab model with (locally) estimated column densities, N_{approx} . In the former, velocity and temperature are held constant along all sightlines, in order to isolate the accuracy of each N_{approx} method. Clockwise from the upper left, N_{approx} is specified by the best-fitting Sobolev length and Sobolev-like (“Sobolev- ρ ”) length (L_{Sob}^k and L_{Sob}^s , respectively; see § 2.3.1), and the Jeans length. The lower left panel shows the results of the only non-local approach, the “six-ray method,” in which the shield factor is calculated for six sight lines using the integrated N_{H_2} and an average over these gives $f_{\text{sh}}(\text{six-ray})$. The overall fractional errors of each $f_{\text{sh}}(N_{\text{approx}})$ are shown in Table 2.

In comparison, the mean error for an increase from six to 16 sightlines was found to be ~ 9 per cent; note that, as in the “six-ray” method described above, the six sightlines were aligned parallel with the Cartesian axes, but in this case, the full calculation was performed – i.e. including density, temperature, and velocity gradients. All of our calculations for $f_{\text{sh},3\text{D}}$ are therefore obtained from averaging over 16 sight lines, which sample evenly in the azimuthal angle and in the cosine of the polar angle.

An additional convergence test was performed to determine the required angular resolution for the mean Sobolev and Sobolev-like lengths ($L^s_{\text{Sob}}, L^s_{\text{Sob}}$). For 25 points selected, again, over the full range of radii considered, the mean error in the spherically averaged Sobolev and Sobolev-like lengths are 15 and 17 per cent for an increase from 16 \rightarrow 25 sightlines, 10 and 11 per cent (25 \rightarrow 49), and 1 and 3 per cent (49 \rightarrow 100), respectively. As a result, 49 sightlines were used in all calculations for the Sobolev and Sobolev-like methods. (Note that these specific numbers are determined by the tiling method we use, which always results in a perfect square for the number of sightlines.)

4 IMPLICATIONS AND CAVEATS

4.1 Cooling and collapse in simulated haloes

In the preceding section, we have shown that common approaches to model self-shielding in simulations can introduce inaccuracies of over an order of magnitude in the H₂ dissociation rate, depending on the level of the shielding and on the method being used. Because the cooling properties of metal-free gas below 10^4 K depend sensitively on the H₂ abundance, errors in the dissociation rate can significantly affect the thermal and dynamical histories of gas in haloes under UV irradiation. In order to quantify such errors, and to specify *when* inaccurate values of f_{sh} will have the greatest impact, we show in Figure 8 the H₂-cooling and dynamical time-scales, given by:

$$\tau_{\text{dyn}} = \sqrt{\frac{3\pi}{16G\rho}}, \quad (11)$$

$$\tau_{\text{cool}} = \frac{(3/2)nk_{\text{B}}T}{|\Lambda_{\text{H}_2}|}, \quad (12)$$

as functions of radius in the five halo outputs. As in the original simulations, we employ the H₂-cooling rate, Λ_{H_2} , provided by Galli & Palla (1998); here, G and k_{B} are the gravitational and Boltzmann’s constant, respectively.

For all radii considered thus far, $0.1 < R < 10$ pc, Figure 8 shows that the dynamical time exceeds the H₂-cooling

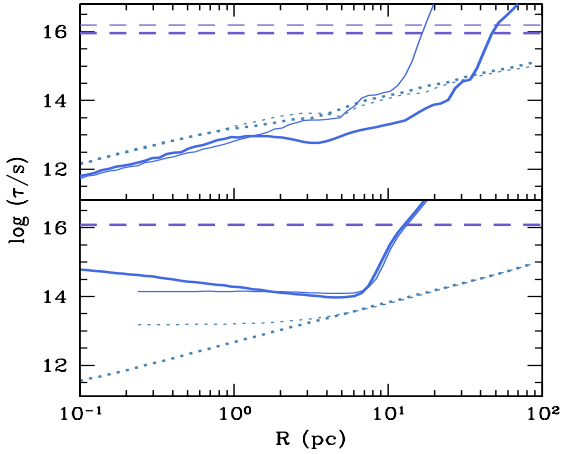


Figure 8. *Upper panel:* spherically averaged H_2 -cooling (solid curves) and dynamical (dotted curves) time-scales are shown for the cold haloes; the Hubble time for each output is shown by horizontal (dashed) lines, with the same cosmological parameter choices as in SBH10, $(\Omega_m, \Omega_\Lambda, h) = (0.279, 0.721, 0.701)$. Thick and thin curves denote the results for outputs 1 and 5, respectively. (The dynamical time-scales are nearly identical for these outputs, making the thick and thin curves indistinguishable.) The results for output 2 are nearly identical to those of output 1, and have been omitted for clarity. *Lower panel:* same as above for the hot haloes, with thick (thin) curves denoting the time-scales for output 3 (4).

time in each of the cold haloes (as expected). More importantly, these time-scales are comparable – i.e. within an order of magnitude – in both hot and cold haloes at $R \lesssim 10$ pc (with the exception of output 3, where the cooling time becomes much longer outside the range $2 \lesssim R \lesssim 10$ pc). Because $\tau_{\text{cool}} < \tau_{\text{dyn}}$ is required for H_2 -cooling to impact the dynamics of these clouds, it is precisely in regions where these time-scales are similar that inaccurate values of the dissociation rate may qualitatively change the history of a simulated cloud. This will indeed be the case, as long as photodissociation and shielding are both non-negligible. For example, if the approximated f_{sh} is too large and the H_2 -cooling rate therefore erroneously low, the collapse of overdense clumps in the halo (ultimately leading to formation of protostellar objects) may be erroneously delayed. Conversely, if the adopted model overestimates shielding, H_2 -cooling may allow for collapse sooner (on smaller scales) than would be possible with the accurate dissociation rate.

In order to further address how errors in the approximate f_{sh} may impact the history of a simulated halo, we consider the “critical flux,” studied by SBH10. It is well known that a sufficiently strong LW flux can suppress H_2 -cooling entirely, keeping the gas in these haloes close to its virial temperature, $T \approx 10^4$ K, providing that it remains un-enriched in metals. There is a sharp bifurcation in the cooling behaviour around the threshold intensity, $J_{\text{crit},21}$, below which the gas is able to reach \sim a few hundred Kelvin via H_2 -cooling (outputs 1, 2, and 5), while haloes irradiated with a super-critical flux will remain H_2 -poor (outputs 3 and 4). From the full suite of simulations, SBH10 found a critical intensity $J_{\text{crit},21} = 10^{4-5}$, in the usual units (here and throughout this discussion, the results are quoted for an

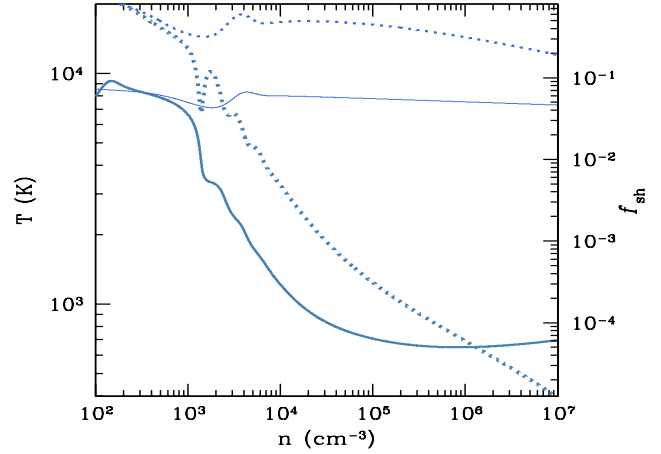


Figure 9. Evolution of gas temperature (solid curves and labels on left) and f_{sh} (dashed curves and labels on right) of collapsing gas in a halo with $T_{\text{vir}} \gtrsim 10^4$ K, are obtained from the spherical collapse model. Both are shown for runs with intensities, J_{21} , just above (thin curves) and below (thick curves) the critical threshold, $J_{\text{crit},21}$. The shield factor is obtained from the modified fitting formula, equation (10), and $J_{\text{crit},21} = 1.4 \times 10^3$. By contrast, if equation (9) is used, $J_{\text{crit},21} = 4.3 \times 10^3$ and the bifurcation around threshold flux occurs at $f_{\text{sh}} \approx 0.1$. The incident spectrum is modeled as that of a blackbody with $T = 10^5$ K and the temperature of the gas is initialized at the virial temperature of the halo. For more on the specifics of the spherical collapse model, the reader is referred to SBH10 and references therein.

incident blackbody spectrum with $T_{\text{BB}} = 10^5$ K, relevant for direct H_2 photodissociation). These results were refined with the use of a one-zone spherical collapse model (for details see SBH10, Omukai et al. 2008), and the threshold intensity was then found to be $J_{\text{crit},21} = 1.2 \times 10^4$.

To further investigate the implications of inaccurate self-shielding models, we have repeated the one-zone calculations in SBH10, altering only how f_{sh} is specified. First, we adopt the more accurate expression given by DB96, equation (9), rather than their power-law fit, equation (8), employed by SBH10. As in the original study, the H_2 column density is still specified by the Jeans length (the only viable option for zero-dimensional models without additionally computing gradients). The specific intensity, J_{LW} , is then varied iteratively with a Newton–Raphson scheme and the critical threshold is found to be $J_{\text{crit},21} = 4.3 \times 10^3$. This reduction in the intensity required to suppress cooling owes to the temperature dependence of equation (9), which more accurately models decreased shielding due to line-broadening than the power-law. Next, we alter the expression for f_{sh} as described in § 3.1 (with $\alpha = 1.1$), and find $J_{\text{crit},21} = 1.4 \times 10^3$. Again, the more accurate fit at high temperatures leads to significantly weaker shielding in the early stages of collapse. The evolution of both temperature and the shield factor as functions of density are shown in Figure 9.

Importantly, because we have employed the Jeans length to estimate N_{H_2} , the dissociation rate is still likely underestimated by a factor of $\gtrsim 2$ at $f_{\text{sh}} \lesssim 10^{-3}$ (see the upper left panel of Figure 7). As a result, the critical intensity quoted here – reduced by a factor of $\approx 3 \times 2 = 6$

– is still an *upper limit*; the full reduction is thus about an order of magnitude. Indeed, SBH10 showed that if one entirely ignores self-shielding (i.e. the optically thin limit), then $J_{\text{crit},21} = 4.4 \times 10^2$ – apparently when self-shielding is treated more accurately, it only modestly increases this value.

This reduction in $J_{\text{crit},21}$ illustrates how the self-shielding approximations can dramatically impact the thermal history of a simulated halo. Furthermore, this may also have interesting cosmogonical implications, suggesting that a larger fraction of haloes than previously thought will see a supercritical flux in the spatially fluctuating UV background (UVB). It has been suggested (see SBH10 and references therein) that gas irradiated by a supercritical flux may avoid fragmentation on small scales, provided that it does not become metal-enriched (see Omukai et al. 2008, for the relevant metallicity threshold), and this may provide a possible mechanism by which primordial gas could collapse directly to form massive black holes, $10^{4-6} M_{\odot}$. However, with the original high $J_{\text{crit},21}$ value, it has also been shown (Dijkstra et al. 2008) that only one in $\approx 10^6$ haloes – only those with an unusually bright and close neighbour – will see a sufficiently high flux. The direct collapse scenario requires that the gas furthermore remain un-polluted by metals and efficiently shed its angular momentum. As a result, it is likely that only a small fraction of even these close halo pairs will form supermassive black holes. The reduction of the $J_{\text{crit},21}$ value will significantly increase the number of candidates for objects that avoid H_2 -cooling and fragmentation, and makes this scenario much more viable.

4.2 Internal and external modification of the radiation field by HI

The results presented thus far may be altered by atomic H Lyman series absorption either within the haloes, where this provides an additional means of shielding H_2 , or in the IGM, where the spectrum of the UVB is modified by the high HI optical depth prior to reionization.

In the first case, suppression of the H_2 dissociation rate becomes significant if large HI column densities are present, $N_{\text{HI}} \gtrsim 10^{23} \text{ cm}^{-2}$. To quantify the impact this has on our results for k_{diss} , we have repeated the three-dimensional calculations with the first nine Lyman lines contributing to the optical depth of each slab. Note that, while the $\text{Ly}\alpha$ transition (10.2eV) lies outside of the LW wavelength range ($\gtrsim 11.2\text{eV}$), it is nevertheless included, because at large N_{HI} its damping wings protrude into the LW band, and contribute to LW shielding.

In the SBH10 haloes, neutral column densities of $10^{21-22} \text{ cm}^{-2}$ are typical at $R \sim 5 - 10 \text{ pc}$, increasing to $10^{23-24} \text{ cm}^{-2}$ at radii smaller than a few pc. In these densest regions, the dissociation rate is decreased by up to a factor of ~ 2.5 in both cold and hot haloes. We find that the numerical results for $f_{\text{sh}}(N_{\text{H}_2}, N_{\text{HI}}, T)$ are well approximated by an analytic expression of the form $f_{\text{sh},\text{H}_2} \times f_{\text{sh},\text{HI}}$, where f_{sh,H_2} is the fit for self-shielding in equation 10 (with $\alpha = 1.1$) and $f_{\text{sh},\text{HI}}$ is the expression provided by Wolcott-Green & Haiman (2011) for HI shielding:

$$f_{\text{sh},\text{HI}} = \frac{1}{(1 + x_{\text{HI}})^{\beta}} \times \exp(-\gamma x_{\text{HI}}). \quad (13)$$

Adopting the same coefficients as in the original expression, $\beta = 1.6$, $\gamma = 0.15$ and $x_{\text{HI}} = N_{\text{HI}}/2.85 \times 10^{23} \text{ cm}^{-2}$, we find that $f_{\text{sh},\text{H}_2} \times f_{\text{sh},\text{HI}}$ is accurate to within a factor of two in the relevant column density and temperature ranges: $10^{13} < N_{\text{H}_2} < 10^{21} \text{ cm}^{-2}$, $10^{22} < N_{\text{HI}} < 10^{24} \text{ cm}^{-2}$, and $500 < T < 5 \times 10^3 \text{ K}$. Note that this degree of accuracy is perhaps surprising, given that the fit $f_{\text{sh},\text{HI}}$ was originally developed for HI shielding of ground state H_2 populations; for more details on this method for approximating the (non-linear) effect of combined shielding by H_2 and HI, the reader is referred to Wolcott-Green & Haiman (2011).

The shape of the UVB spectrum is also modified by HI in the IGM, as photons traveling over cosmological distances will be absorbed once they redshift into resonance with a Lyman line. Subsequently, the original photon will be replaced, in a radiative cascade, by several lower-energy photons⁷. This results in a characteristic sawtooth shape of the spectrum (see Haiman et al. 1997 and HAR00 for a detailed discussion). To investigate how this modulation of the incident flux impacts our results, we have recalculated f_{sh} , assuming a single (isothermal and static) slab of gas irradiated on one side, with the input spectrum given by $J_{\nu} = J_{21} \times \text{sawtooth modulation}$ ($z = 15$), adopted from HAR00 (from the model shown in their Figure 1). We have found that the self-shielding behaviour is insensitive to this modification – f_{sh} is decreased by ~ 10 per cent over a wide range of temperatures ($10^2 - 10^4 \text{ K}$), column densities ($N_{\text{H}_2} < 10^{24} \text{ cm}^{-2}$), and irrespective of the assumed H_2 level populations. While the SBH10 halo outputs are at redshifts somewhat lower than $z = 15$, the magnitude of the sawtooth effect decreases over time in the HAR00 model, due to the redshift-dependent source formation rate; thus, the decrease in f_{sh} quoted above is in fact an upper limit.⁸

4.3 Anisotropic LW flux

In taking the average dissociation rate over all sight lines for the 3D calculations, we have thus far assumed isotropy of the incident LW flux. This is likely a good approximation when the flux is close to the global mean background, and is dominated by a large number of distant sources. However, if the radiation field is strong, i.e. the halo has one (or a few) bright neighbours, then the flux will be anisotropic, with f_{sh} for individual sight lines pointing toward the nearby source most important. Indeed, the latter case is particularly relevant in the context of the critical flux discussed above, as supercritical intensities, $J_{21} \gtrsim 10^3$, are likely to be well above the cosmic mean (Dijkstra et al. 2008).

Let us consider the ramifications of anisotropic incident

⁷ In the case of $\text{Ly}\alpha$, the original photon may only be lost through two-photon decays. However, this line is outside of the wavelength range of interest for H_2 anyway.

⁸ It is worth noting that the optically thin rate is decreased by a factor of ~ 10 compared to that given by the unmodified spectrum. However, we are primarily interested here in the self-shielding behaviour, rather than in the changes to the model-dependent magnitude of the intergalactic UVB.

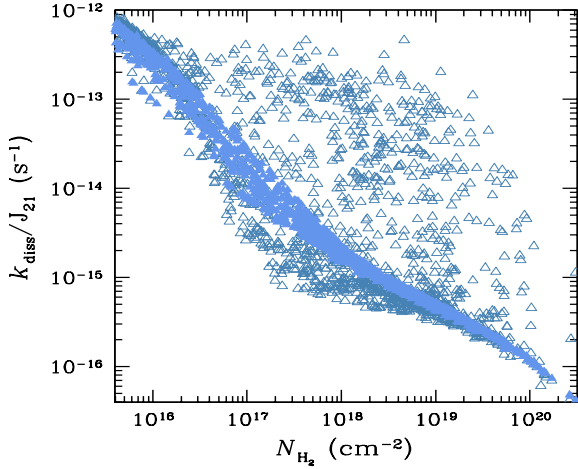


Figure 10. Comparison of the numerically calculated photodissociation rate coefficient along individual sight lines emanating from ~ 100 points at $1 < R < 10$ pc in output 5 (open triangles) with those obtained when the gas is assumed to be both static and isothermal (closed triangles).

flux for self-shielding models in the context of gas velocity and temperature gradients. As shown in Figure 6, the shield factor for a given sightline may be altered dramatically by variations in the gas velocity or temperature in that direction. This point is further illustrated in Figure 10, in which f_{sh} for individual sight lines emanating from 100 points are shown in comparison with those when both velocity and temperature gradients are artificially switched off. (See § 3.2–3.3 for details of how the observed discrepancies arise.) Here, we see that the dissociation rate fluctuates by \approx two orders of magnitude in different directions. The rates will also be incorrect by up to several orders of magnitude if one makes the standard assumption of static and isothermal shielding gas. (On the other hand, the relative accuracy of each N_{approx} along individual sight lines would not be particularly informative here, largely because simulations in which the radiation field is both spatially and angular resolved typically do not rely on the type of local estimates for N_{H_2} described above.)

4.4 Uncertainty in the rovibrational distribution

In the most general case, one would have to consider the non-equilibrium H_2 population levels produced during gas-phase H_2 formation, as well as the time-dependent cascades among levels. This, in general, would produce a population level distribution that is different than assumed in DB96. Absent such a fully time-dependent calculation of the rovibrational level populations, we have thus far made the simplifying assumption that rotational states within the ground vibrational state are populated according to a Boltzmann distribution and that the abundance of H_2 in higher vibrational states are negligible. However, because the level populations play an important role, particularly in the temperature dependence of the dissociation rate (see § 3.1–§ 3.3), a more detailed examination of this assumption is in order.

It has already been noted that thermal populations are not established in higher vibrational levels until particle den-

sities $n_{\text{crit}} \sim 10^{6-7} \text{ cm}^{-3}$ are reached (see, e.g. Table 1 in LPF99), so there is little uncertainty that populations in $v > 0$ are negligible for the SBH10 haloes, at least at the most relevant stages of collapse that we considered here. However, higher rotational levels within $v = 0$ also thermalize at higher critical densities, and because the collisional cross-sections depend strongly on temperature, so also do the values of n_{crit} . As an example, consider the S(2) transition (for $v = 0$), for which the critical density at 500, 1000, and 2000 K, respectively, is $n_{\text{crit}} = 1.2 \times 10^4, 1.7 \times 10^3, 2.5 \times 10^2 \text{ cm}^{-3}$ (LPF99). Given that the most rarefied regions of the haloes $n < 10^2 \text{ cm}^{-3}$ are typically at temperatures of \sim several thousand Kelvin (see Figure 1), most likely the rotational populations within $v = 0$ will indeed tend to a Boltzmann distribution. None the less, we have repeated our three-dimensional calculations with populations in $J = 0, 1$ only, and with a fixed ortho:para ratio of 3:1. The results are compared to the original $f_{\text{sh},3\text{D}}$ in the left panel of Figure 11. Because restricting the molecules to occupy only $J = 0, 1$ is, in effect, similar to setting the temperature very low ($T \lesssim 100$ K) in the LTE model, it is not surprising that the shield factor is smaller in this case. The clear dip in the results above $f_{\text{sh},3\text{D}} \gtrsim 5 \times 10^{-4}$ arises simply because the optical depth decreases toward hotter regions of these haloes. At the smallest values of f_{sh} , the local temperature is only a \sim few hundred Kelvin, and as a result, the ground state results do not differ dramatically from the original (LTE) calculations. In the right panel of Figure 11, the ground state results are also compared to those from equation (9), confirming that the DB96 expression is indeed a better fit to the numerical results in a rotationally-cold gas.

4.5 Fluorescent excitation of H_2

All calculations to this point have implicitly assumed that each LW photon is permanently removed from the radiation field upon absorption by H_2 . However, on average only 10 – 15 per cent of absorption (“pumping”) events result in dissociation, while the remainder are followed by transitions to another bound vibrational state. In a “resonant scattering,” a single decay returns the molecule directly to the initial rovibrational state ($v, J = v'', J''$) and the original LW photon is re-emitted. More frequently, UV-pumping is followed by a cascade through multiple levels, resulting in both infrared fluorescence and emission of a LW photon (with different-energy) in the electronic transition. It is then possible for this (or the resonantly scattered) photon to be reabsorbed, a process which has not been accounted for thus far. If the optical depth to the re-emitted photon is non-negligible this requires a non-trivial modification in our calculations of k_{diss} . However, recall that only H_2 transitions originating in the $v = 0$ are included; as a result, to first order, we need only consider photons emitted in decays directly back to the ground vibrational state. The fraction of downward transitions to each bound vibrational level are quantified by Shull (1978); they find that ~ 15 per cent of all absorption events originating in $v = 0$ result in decays directly back to $v'' = 0$ (see their Table 1). Therefore, accounting for the optical depth to re-emitted photons represents a small correction to our results.

There is an additional complication, however, if the gas is irradiated by a very strong UV flux, in which the cas-

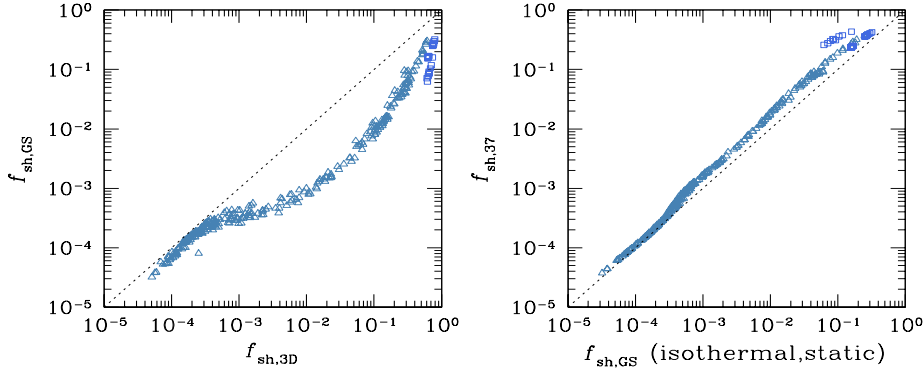


Figure 11. *Left panel:* comparison of full three-dimensional calculations with LTE populations, $f_{\text{sh},3\text{D}}$, to those in which only the ortho and para ground states of the molecules are populated, with a fixed ortho:para ratio of 3:1. *Right panel:* results of the ground-state calculation are compared to those from the DB96 fitting formula, equation (9). In the latter case, the mean ($f_{\text{sh},37}$) over all 16 sight lines is shown, with velocity and temperature gradients artificially switched off, in order to isolate the accuracy of the fitting formula.

cade to $v'' = 0$, J'' may be interrupted by absorption of LW photons from $v'' > 0$. However, only in very strong radiation fields, $J_{21} > 10^{5-8}$, are molecules more likely to be “re-pumped” in this way, rather than undergoing radiative transitions to lower rovibrational states (Shull 1978). Therefore, in the present context of an intergalactic UVB, neglecting this multiple pumping mechanism is also justified.

5 SUMMARY AND CONCLUSIONS

We have shown that the results of existing approximations for self-shielding in three-dimensional simulations often introduce large inaccuracies in the optically thick H_2 photodissociation rate. In particular, the approximate results typically underestimate the numerically calculated rate by more than an order of magnitude in low density regions, $n < 10^4 \text{ cm}^{-3}$, or where the true shield factor is $10^{-3} \lesssim f_{\text{sh},3\text{D}} \lesssim 1$. At higher densities, we find that the approximate methods are much more accurate, with typical errors of ~ 25 per cent. There are a number of factors contributing to the discrepancies between the approximate and numerical results, which are summarized below:

(i) The largest source of error in the approximate methods is the analytic fit for f_{sh} provided by DB96. While this oft-used expression is reasonably accurate at low temperatures, we find that it overestimates shielding by a large factor at temperatures above a few hundred Kelvin (for a gas in LTE). The resulting deviations from our numerical results are most apparent at $n < 10^4 \text{ cm}^{-3}$, as these low-density regions typically have not cooled below $\sim 500 - 10^3 \text{ K}$ in the SBH10 simulations. However, we have found that a very simple modification to the DB96 expression (see equation 10) improves the agreement with our numerical results to within ~ 15 per cent.

(ii) Nearly all existing approaches to approximate f_{sh} are based on a static slab model for the shielding gas, which neglects the diminished optical depth due to frequency shifts of the H_2 resonances in the presence of velocity gradients. We find that these frequency shifts do not greatly

alter the dissociation rate in the SBH10 haloes, largely because the gas motions in these simulations are dominated by a coherent flow toward the dense core, rather than (supersonic) turbulence; therefore, typically only a small number of sightlines from a given point see large changes in the bulk velocity. The resulting increase in the spherically averaged rate is only significant (~ 65 per cent) in the range $4 \times 10^{-4} \lesssim f_{\text{sh}} \lesssim 2 \times 10^{-2}$, and elsewhere is generally negligible.

(iii) We find that gas temperature gradients can alter the self-shielding behavior dramatically via changes in both the thermal line widths and in the rovibrational level populations. In this case, the dissociation rate may be either increased or decreased, depending on the sign of the temperature gradient along each sightline. However, the effect again is smaller for the spherically averaged rate, and tends to make shielding stronger in the haloes we analyze, largely counteracting any changes due to frequency shifts. Taken together, temperature and velocity gradients therefore typically only introduce a factor of $\lesssim 2$ scatter in spherically averaged rate.

(iv) Finally, we have evaluated several approaches to estimate the shielding column density in simulations (and one-zone models). The most common of these is based on the assumption that the characteristic length scale for shielding is of order the local Jeans length. In agreement with SBH10, we find that this method is very accurate at densities $n \gtrsim 10^{4-5} \text{ cm}^{-3}$, but underestimates the optically thick rate by \gtrsim an order of magnitude at lower densities. However, we show that two less commonly used methods provide reasonably accurate estimates of the shielding column at all densities we consider, and are computationally inexpensive, relying again only on local properties of the gas. These are based on the Sobolev length and a variation of the Sobolev length based on the density – rather than velocity – gradient; both yield more accurate results for f_{sh} than the Jeans length method in low-density regions, with essentially unbiased scatter around the true value. We also show that a “six-ray” method, based on integrating the column density in only six directions is extremely accurate, deviating

from the “exact results” only due to the effects of temperature and velocity gradients. However, this non-local method comes with a larger computational expense.

In addition to the factors enumerated above, HI shielding of H₂ also causes the “true” dissociation rate to deviate from the results of approximate treatments, which most often neglect this additional shielding. We find that this effect can be well modeled by a simple analytic prescription provided by Wolcott-Green & Haiman (2011). The simple fitting formulae we provide can be trivially incorporated into future three-dimensional simulations, to improve the speed and accuracy of calculations of the H₂-photodissociation rate.

Finally, using the same (one-zone) spherical-collapse model employed by SBH10, we show that the critical LW flux J_{crit} required to keep $T_{\text{vir}} \gtrsim 10^4\text{K}$ haloes H₂-poor is reduced by about an order of magnitude as a result of improved accuracy in the shielding factor. This serves to illustrate an important conclusion of our study: the cooling properties – and thereby the dynamical history – of (metal-free) gas in simulated haloes depend sensitively on the adopted self-shielding model. In particular, the reduction in J_{crit} implies that H₂-cooling is suppressed in many more of these haloes, thus increasing the potential sites for direct formation of SMBHs in the early universe.

6 ACKNOWLEDGMENTS

We thank Cien Shang for helpful discussions, and for sharing the simulation data. We are also grateful to the developers of the analysis toolkit *YT* (<http://yt.enzotools.org>), which facilitated analysis and visualization of the *ENZO* data. We acknowledge support from NSF grants AST-05-07161, AST-05-47823, AST-09-08390, and AST-10-08134, as well as computational resources from NASA, NSF Teragrid, and Columbia University’s Hotfoot cluster.

REFERENCES

- Abel T., Haiman Z., 2000, in F. Combes & G. Pineau Des Forets ed., *Molecular Hydrogen in Space The Role of H₂ Molecules in Cosmological Structure Formation*. pp 237–+
- Abgrall H., Le Bourlot J., Pineau Des Forets G., Roueff E., Flower D. R., Heck L., 1992, *A&A*, 253, 525
- Abgrall H., Roueff E., Drira I., 2000, *A&AS*, 141, 297
- Abgrall H., Roueff E., Launay F., Roncin J. Y., Subtil J. L., 1993a, *A&AS*, 101, 273
- Abgrall H., Roueff E., Launay F., Roncin J. Y., Subtil J. L., 1993b, *A&AS*, 101, 323
- Ahn K., Shapiro P. R., 2007, *MNRAS*, 375, 881
- Bromm V., Loeb A., 2003, *ApJ*, 596, 34
- Bryan G. L., 1999, *Comput. Sci. Eng.*, Vol. 1, No. 2, p. 46–53, 1, 46
- Ciardi B., Ferrara A., Abel T., 2000, *ApJ*, 533, 594
- de Jong T., Boland W., Dalgarno A., 1980, *A&A*, 91, 68
- Dijkstra M., Haiman Z., Mesinger A., Wyithe J. S. B., 2008, *MNRAS*, 391, 1961
- Draine B. T., Bertoldi F., 1996, *ApJ*, 468, 269
- Federman S. R., Glassgold A. E., Kwan J., 1979, *ApJ*, 227, 466
- Field G. B., Somerville W. B., Dressler K., 1966, *ARA&A*, 4, 207
- Flower D. R., Harris G. J., 2007, *MNRAS*, 377, 705
- Galli D., Palla F., 1998, *A&A*, 335, 403
- Glover S. C., Savin D. W., Jappsen A., 2006, *ApJ*, 640, 553
- Glover S. C. O., Brand P. W. J. L., 2001, *MNRAS*, 321, 385
- Glover S. C. O., Brand P. W. J. L., 2003, *MNRAS*, 340, 210
- Glover S. C. O., Clark P. C., 2011, *ArXiv e-prints*
- Glover S. C. O., Mac Low M., 2007a, *ApJS*, 169, 239
- Glover S. C. O., Mac Low M., 2007b, *ApJ*, 659, 1317
- Gnedin N. Y., Tassis K., Kravtsov A. V., 2009, *ApJ*, 697, 55
- Greif T. H., Glover S. C. O., Bromm V., Klessen R. S., 2010, *ApJ*, 716, 510
- Haiman Z., Abel T., Rees M. J., 2000, *ApJ*, 534, 11
- Haiman Z., Rees M. J., Loeb A., 1997, *ApJ*, 476, 458
- Heck E. L., Flower D. R., Le Bourlot J., Pineau des Forets G., Roueff E., 1992, *MNRAS*, 258, 377
- Hollenbach D. J., Werner M. W., Salpeter E. E., 1971, *ApJ*, 163, 165
- Hosokawa T., Inutsuka S., 2005, *ApJ*, 623, 917
- Hosokawa T., Inutsuka S., 2006, *ApJ*, 646, 240
- Johnson J. L., Greif T. H., Bromm V., 2008, *MNRAS*, 388, 26
- Johnson J. L., Khochfar S., Greif T. H., Durier F., 2011, *MNRAS*, 410, 919
- Le Bourlot J., Pineau des Forêts G., Flower D. R., 1999, *MNRAS*, 305, 802
- Le Bourlot J., Pineau Des Forets G., Roueff E., Flower D. R., 1993, *A&A*, 267, 233
- Machacek M. E., Bryan G. L., Abel T., 2001, *ApJ*, 548, 509
- Machacek M. E., Bryan G. L., Abel T., 2003, *MNRAS*, 338, 273
- Mesinger A., Bryan G. L., Haiman Z., 2006, *ApJ*, 648, 835
- Mesinger A., Bryan G. L., Haiman Z., 2009, *MNRAS*, 399, 1650
- Norman M. L., Bryan G. L., 1999, in S. M. Miyama, K. Tomisaka, & T. Hanawa ed., *Numerical Astrophysics Vol. 240 of Astrophysics and Space Science Library, Cosmological Adaptive Mesh Refinement*. pp 19–+
- Omukai K., 2001, *ApJ*, 546, 635
- Omukai K., Nishi R., 1999, *ApJ*, 518, 64
- Omukai K., Schneider R., Haiman Z., 2008, *ApJ*, 686, 801
- O’Shea B. W., Bryan G., Bordner J., Norman M. L., Abel T., Harkness R., Kritsuk A., 2004, *ArXiv Astrophysics e-prints*
- Ricotti M., Gnedin N. Y., Shull J. M., 2001, *ApJ*, 560, 580
- Safranek-Shrader C., Bromm V., Milosavljević M., 2010, *ApJ*, 723, 1568
- Shang C., Bryan G. L., Haiman Z., 2010, *MNRAS*, 402, 1249
- Shull J. M., 1978, *ApJ*, 219, 877
- Sobolev V. V., 1957, *Sov. Astron.*, 1, 678
- Stecher T. P., Williams D. A., 1967, *ApJL*, 149, L29+
- Turk M. J., Smith B. D., Oishi J. S., Skory S., Skillman S. W., Abel T., Norman M. L., 2010, *ApJS*, accepted
- Wise J. H., Abel T., 2007, *ApJ*, 671, 1559

- Wise J. H., Abel T., 2008a, ApJ, 684, 1
Wise J. H., Abel T., 2008b, ApJ, 685, 40
Wolcott-Green J., Haiman Z., 2011, MNRAS, 412, 2603
Yoshida N., Abel T., Hernquist L., Sugiyama N., 2003,
ApJ, 592, 645
Yoshida N., Oh S. P., Kitayama T., Hernquist L., 2007,
ApJ, 663, 687
Yoshida N., Omukai K., Hernquist L., Abel T., 2006, ApJ,
652, 6